J Therm Spray Tech
https://doi.org/10.1007/s11666-026-02193-7

ORIGINAL RESEARCH ARTICLE

Comparative Study of CGS, HVAF and VPS Coatings on Single Crystal Substrates for Turbine Blade Repair

M. Létang[1] · J. Schmitt[1] · T. Sievert[1] · S. Björklund[2] · S. Joshi[2] · J. Gibmeier[3] · F. Lang[3] · D. Sebold[1] · O. Guillon[1,4] · R. Vaßen[1,5]

Submitted: 9 September 2025 / in revised form: 7 January 2026 / Accepted: 22 January 2026

Abstract The repair of high-value single-crystal turbine blades is essential for both sustainability and cost efficiency, as these components are susceptible to degradation when exposed to extreme operating conditions. This study investigates and compares coatings produced using three different thermal spraying processes, cold gas spraying, high-velocity air-fuel spraying, and vacuum plasma spraying, to identify the optimal method for repair applications requiring subsequent directed recrystallization. The comparison showed that VPS coatings offer the most promising properties: They exhibit the lowest oxygen content, near-zero residual stress, and superior adhesion and successfully achieved the required 2 mm coating thickness without delamination. While CGS and HVAF were limited in achievable thickness, the resulting columnar grain structure of the VPS coating may pose a challenge for the intended directed recrystallization process.

Keywords adhesion strength · CMSX-4 coating · cold gas spraying · high-velocity air-fuel spraying · residual stresses · single crystal repair · vacuum plasma spraying

✉ M. Létang
maike.letang@rwth-aachen.de

[1] Institute of Energy Materials and Devices (IMD-2), Forschungszentrum Jülich GmbH, 52425 Jülich, Germany

[2] University West, 46186 Trollhättan, Sweden

[3] Institute for Applied Materials (IAM-WK), Karlsruhe Institute of Technology (KIT), Engelbert-Arnold-Str. 4, 76131 Karlsruhe, Germany

[4] Jülich Aachen Research Alliance: JARA Energy, 52425 Jülich, Germany

[5] Institut für Werkstoffe, Ruhr-Universität Bochum, Bochum, Germany

Introduction

Single-crystal turbine blades constructed from nickel-based superalloys, such as CMSX-4, are crucial for gas turbine applications due to their superior high-temperature properties, which are primarily attributed to their γ/γ' microstructure. Nonetheless, these components are vulnerable to a range of damage mechanisms, especially at the edges. The repair of these high-value components is essential for both ecological sustainability and economic efficiency. A complete set of high-pressure turbine blades (60-80 blades) is worth between 400,000 and 700,000 US dollars (Ref 1). Given these high costs and the considerable time required for production, the development of effective repair strategies is advantageous. However, it presents significant challenges, as the restoration of the single-crystal microstructure in the repair zone is imperative. (Ref 2, 3)

Since the late 1960 s, various welding techniques, including gas tungsten arc welding, tungsten inert gas welding, electron beam welding, and laser welding, have been explored for repairing polycrystalline superalloy components (Ref 4). However, these methods present significant challenges, particularly due to large heat-affected zones that can lead to geometric deviations and distortion, as well as susceptibility to cracking. The weldability of these alloys decreases with increasing aluminum and titanium content; specifically, alloys with a combined content exceeding 4 wt.% are considered difficult or impossible to weld. (Ref 5-7)

In the 1980 s, Rolls-Royce introduced laser-based surface repair coating for polycrystalline aircraft turbine components, utilizing nickel superalloys like Inconel 718 (Ref 7-9). Complete repair of single-crystal components is currently unachievable, resulting in their restoration to a

Published online: 10 April 2026

polycrystalline state, which reduces lifespan (Ref 10). Gäumann et al. (Ref 11, 12) developed the epitaxial laser metal forming (E-LMF) technique, enabling the deposition of single-crystal repair layers on single-crystal substrates. Studies (Ref 4, 10, 13, 14) indicate that, with precise process control, other laser techniques can also facilitate the repair of single-crystal materials. These methods allow for high temperature gradients and rapid solidification, promoting epitaxial growth. Nonetheless, issues such as grain formation and cracking persist, and most research focuses on creating isolated laser tracks, which limits the repair area. As a result, only limited repair of single-crystal turbine blades is currently feasible (Ref 4, 15).

Thermal spraying as a repair method has been extensively documented in scientific literature (Ref 16-22). Moreover, patents, particularly for turbine blade and high-pressure turbine component restoration, show the importance of the topic (Ref 23, 24]. Thermal spraying encompasses different processes that can be used for repair applications. These processes, such as cold gas spraying (CGS), high velocity air-fuel (HVAF) spraying, and vacuum plasma spraying (VPS), must be capable of depositing dense coatings with low oxygen content. In CGS, powder particles are accelerated to supersonic velocities using a convergent–divergent nozzle with a compressed process gas at relatively low temperatures. The particles undergo plastic deformation upon impact, creating a bond with the substrate (Ref 25). CGS is widely used for repair purposes, as emphasized in the summaries of repair methods provided by Yin et al. (Ref 26) and Raoelison et al. (Ref 27). CGS has proven effective in various applications, for example, in repairing military aircraft exterior components (Ref 28). The study shows successful restoration of aluminum 2024-T6 parts using 6061-Al powder, with repaired components often exceeding required load capacities. Fiebig et al. (Ref 20) demonstrated the fabrication of three mm thick IN738 coatings using CGS on laser-textured IN738 substrates. These nickel-based superalloys are commonly used in high-temperature applications.

HVAF spraying utilizes the combustion of fuel and compressed air to generate a high-velocity jet that accelerates powder particles (Ref 29). The process temperatures are moderate, resulting mostly in partially molten particles. Overall, there are relatively few studies in the literature that analyze the suitability of the HVAF process as a repair method. HVAF spraying has shown promise in Ti-6Al-4 V repairs, achieving high-density coatings with less than 0.5% porosity and wear resistance comparable to substrate material (Ref 16). Another study by Khamsepour et al. (Ref 30) examined the potential of the inner diameter-high velocity air fuel (ID-HVAF) process for repairing Ti-6Al-4 V. However, the process resulted in an undesirable phase transformation, and the produced samples exhibited higher porosity compared to the cold-sprayed reference samples.

In VPS, an electric arc between a cathode and anode creates an ionized plasma jet reaching temperatures in the order of 10,000 °C (Ref 29). The process takes place in a low-pressure chamber to prevent oxidation, allowing for dense, oxide-free coatings. Vacuum Plasma Spraying (VPS) research, though limited, shows potential for single-crystal CMSX-4 substrate restoration. Optimal coating parameters and a subsequent hot isostatic pressing resulted in dense coatings with ideal γ/γ' microstructure (Ref 17).

Overall, these thermal spraying techniques demonstrate significant potential for component repair, as they can produce dense coatings with low oxygen content, which is a critical criterion for repair applications in this context. Therefore, in this study, CGS, HVAF and VPS are investigated for their suitability for the repair of single crystal CMSX-4 turbine blades. At this point, it should be mentioned that, since the repair coating is polycrystalline in its as-sprayed state, it is intended to be transformed into a single crystal through a directional recrystallization treatment after these investigations. For this step, a fine-grained structure is beneficial as it serves as the driving force for the directed recrystallization. Numerous studies (Ref 31–33) in the literature have effectively utilized this method to produce columnar or single-crystal grain structures in a range of materials, including nickel alloys. The primary focus in this study is to conduct a comparative analysis of the coatings optimized in preceding steps. Depending on the method used and the spraying parameters, thermally sprayed coatings may exhibit various defects, such as pores, oxide inclusions, and unmolten particles, which can negatively affect the coating properties. Moreover, residual stresses are present in thermally sprayed coatings, which can potentially lead to cracks, delamination, or distortions, thereby impairing the performance and lifespan of the coated components (Ref 34, 35). The development of residual stresses in thermally sprayed coatings can be primarily attributed to three main causes. Quenching stresses (σ_q) manifest as tensile residual stresses in the coating, resulting from the constrained contraction of hot splats on the cold substrate (Ref 36, 37). Additionally, thermal residual stresses (σ_{th}) develop during the cooling process due to differences in thermal expansion coefficients between the substrate and coating material (Ref 34, 38). Technologies utilizing high kinetic energy, such as cold gas spraying, generate additional peening stresses (σ_{peen}) through plastic deformation of the material,

thereby inducing compressive residual stresses in the coating, similar to the effects observed in shot peening (Ref 39, 40). To determine the residual stresses in a coating the incremental hole drilling method standardized according to ASTM E837-20 (Ref 41) can be used. The evaluation of stress levels is important, as thicker coatings with higher stresses tend to fail prematurely. This occurs because the stored elastic energy increases with coating thickness, ultimately leading to delamination when the interfacial strength is exceeded. This failure can occur either during the coating process or during subsequent operation (Ref 38). When a critical value is exceeded, coating delamination occurs. An increase in interfacial strength can be achieved through methods such as elevated substrate temperatures or improved adhesion through alternative substrate pre-treatment processes (Ref 36, 38). Due to these complex interactions between coating thickness, residual stresses, and interfacial strength, adhesion testing methods such as tensile adhesion tests are essential for evaluating the coating–substrate bond strength. Considering the differences in microstructure, bond strength, and residual stress state of the coatings produced by different processes, this paper aims to address the question of which process is most suitable for the repair application.

Experimental Methods

Sample Production

For the repair application under investigation, both the single crystal substrate and the powder material are made from the same alloy, CMSX-4. This material is commonly used in gas turbine applications as a single-crystal alloy. The chemical composition of the materials was analyzed using inductively coupled plasma mass spectrometry (ICP-OES) (iCAP 7600, Thermo Fisher Scientific, USA), and the results are provided in Table 1. Different powder fractions were used depending on the coating process.

For the experiments, single-crystal substrates with varying geometries were used. Square samples (25 mm x 25 mm x 3 mm) were employed for microstructural characterization (MC), single-splat experiments (SS) and residual stress determination using the incremental hole drilling method (RS). Cylindrical samples with a diameter of 25 mm and a thickness of 3 mm were used for adhesion testing (AT).

Substrate Pretreatment

Different substrate pretreatments were used depending on the coating process, as summarized in Table 2. Grinding with 80-grit sandpaper was used as substrate pretreatment for the CGS process. For HVAF, optimal substrate pretreatment was accomplished solely by laser texturing during process parameter optimization prior to that study. Simple grinding was not sufficient to achieve adequate adhesion, and sandblasting left behind sand particles that would hinder the subsequent planned directional recrystallization. For VPS, a polished substrate was used, as Kalfhaus et al. (Ref 17) demonstrated that preheated polished substrates enable epitaxial growth, which likely provides good adhesion and may offer advantages for subsequent directional recrystallization. Laser texturing was performed using the TruMark 5020 system from Trumpf (Ditzingen, Germany), equipped with an Nd-YAG laser operating at a wavelength of 1064 nm. To prevent oxidation, the process was conducted under an argon atmosphere. Material removal was achieved in pulsed mode with 55% power, a frequency of 45 kHz, and a pulse duration of 80 ns. The laser exposure area had a diameter of 40 µm, and the point spacing in the X- and Y-directions was set to 60 µm, with each point exposed 12 times. Laser texturing was also applied to prepare adhesion samples and for residual stress measurements using the hole drilling method across all processes. This ensured comparable experimental conditions for all tests. The surface roughness of the substrates (R_a and R_{max}) was measured using the Cyberscan CT350 device from cyberTECHNOLOGIES (Eching, Germany) in accordance with DIN EN ISO 4287.

Powder

Depending on the thermal spraying process used, different powder fractions were employed following prior process parameter optimizations (Ref 17, 42, 43). TLS Technik GmbH & CO Spezialpulver KG manufactured both powders using gas atomization, followed by vibration sieving to achieve two distinct particle size distributions. Specifically, a fine fraction and a slightly coarser fraction were

Table 1 Chemical composition of the CMSX-4 substrate and the powder used in this study (in wt.%)

Material/Element	Ni	Co	Cr	Al	W	Re	Ta	Ti	Mo	Hf
Substrate	bas.	9.6	6.4	5.6	6.4	2.9	6.5	1	0.6	0.1
CMSX-4 (< 25 µm)	bas.	9.1	5.9	5.6	5.7	2.7	5.7	1	0.6	0.1
CMSX-4 (25-45 µm)	bas.	9.3	6.4	5.4	6.3	2.8	6.1	1	0.6	0.1

Table 2 Overview of substrate pretreatments used in this study, achieved surface roughness (R_a and R_{max}), and their purpose (microstructural characterization (MC), single-splat experiments (SS), residual stress measurements using the incremental hole drilling method (RS) and adhesion testing (AT))

Substrate pretreatment	R_a in µm	R_{max} in µm	Purpose of use
Grinding	0.53	7.0	CGS (MC, RS, AT)
Polishing	0.02	0.24	VPS (MC, RS, AT)
Laser Texturing	7.36	56.68	HVAF (MC, RS, AT) / CGS (RS, AT) / VPS (RS, AT)

Table 3 Particle size distributions and oxygen contents of the CMSX-4 powders used in this work

Powder	D_{10} in µm	D_{50} in µm	D_{90} in µm	Oxygen content in wt.%
CMSX-4 (< 25 µm)	9	18	29	0.036
CMSX-4 (25-45 µm)	14	41	61	0.014

utilized. The particle size distribution of the powders was measured using laser diffractometry with an LB550 device (Horiba, Japan), while the oxygen content was determined using the LECO ON836 device (LECO Corporation, USA). The particle sizes and oxygen contents of the powders are provided in Table 3. Dx denotes the particle size corresponding to the cumulative frequency of x%. The fine powder fraction was used for coating production via CGS and HVAF, whereas the coarser fraction was employed for coatings produced via VPS. More detailed powder analyses can be found in the following paper (Ref 42), where it has been shown that topologically closed packed (TCP) phases occur more frequently in coarser powder particles, promoting brittle behavior.

Sample Production

The CGS was carried out on the Impact 5/11 system from Impact Innovation GmbH (Rattenkirchen, Germany), using a water-cooled D-24 Laval nozzle. The system is designed with a long pre-chamber (170 mm) to allow for a longer dwell time of the powder, which in turn increases the particle temperature. The powder is injected radially, and nitrogen is used as the carrier gas. The substrates are initially preheated to approximately 300 °C. For this, the spray gun moves across the substrate, heating it via the gas flow without powder injection. The process parameters include a gas temperature of 1100 °C, a gas pressure of 5 MPa, a spray distance of 10 mm, and a robot speed of 500 mm/s. A total of 26 coating cycles were used to achieve a coating thickness of approximately 500 µm.

The HVAF experiments were conducted at the University West in Trollhättan, Sweden. For the coatings, an HVAF system with UltraCoat process control, in combination with an M3 gun from Uniquecoat Technologies (LLC, Oilville, VA, USA), was used. The air-cooled M3 gun is operated with propane as the fuel gas. A dual-nozzle system is employed to achieve higher flame temperatures. Powder delivery is managed via a gravimetric G4 powder feeder (Uniquecoat Technologies, LLC, Oilville, VA, USA), with the powder being injected axially into the combustion chamber. For sample coating, a carousel system is used, and continuous sample cooling is applied. The 5L4 nozzle, combined with higher pressures (compressed air pressure: 0.78 MPa, fuel gas pressure 1: 0.72 MPa, fuel gas pressure 2: 0.79 MPa), along with fine powder, was selected for further experiments (Ref 43). The process parameters include a spray distance of 300 mm, surface speed of 100 m/min, powder feed rate of 10 g/min, and carrier gas flow rate of 45 L/min. A total of 70 coating cycles were applied to achieve the desired coating thickness.

The VPS samples were manufactured using the Oerlikon Metco AG Multi Coat VPS system with the F4 gun (nozzle diameter 7 mm). The substrates were preheated to 1000 °C using plasma, with the temperature monitored at the backside of the substrates via a thermocouple. A plasma gas mixture of 50 NLPM argon and 10 NLPM hydrogen was used, with a current of 640 A applied at a chamber pressure of 60 mbar. For the fabrication of these VPS samples, a spray distance of 250 mm, a gun speed of 100 mm/s, and a powder feed rate of 12% were employed. A total of 4 coating cycles were applied to achieve the desired coating thickness of 500 µm.

Characterization Methods

Metallographic Preparation and Image Analyses

Metallographic cross sections were created to analyze porosity, coating thickness, and microstructural properties, such as phases and grain structure. Following embedding

and cutting, the samples were ground and polished to a final step of 0.05 µm using an ATM Saphir 550 system (Struers GmbH, Germany). If the samples are prepared to determine the grain structure, the last step is carried out for one hour. A Hitachi TM3000 tabletop scanning electron microscope (SEM) (Hitachi High-Technologies Europe GmbH, Krefeld, Germany) was utilized for microstructural examination, focusing on porosity and coating thickness. For high-resolution imaging and energy-dispersive x-ray spectroscopy (EDS) and electron backscatter diffraction (EBSD) analyses, the Gemini SEM 450 (Carl Zeiss AG, Oberkochen, Germany) was employed, equipped with an ULTIM MAX 170 EDS detector and a C NANO detector (Oxford Instruments, Abingdon, United Kingdom). In addition, an EVO 15 from Zeiss (Oberkochen, Germany), equipped with an ULTIM MAX 100 EDS detector from Oxford Instruments, is used for some EDS measurements.

Coating thickness was measured at three different locations at three different SEM images using ImageJ software (Fiji). Additionally, seven random SEM images were taken at a fixed magnification to quantify the porosity. These images were processed into binary format, allowing the determination of the pore fraction within the images. The oxygen content in both the powder and the coatings was determined using an elemental analyzer for oxygen, nitrogen, and hydrogen, the LECO ON836, manufactured by LECO Corporation (St. Joseph, USA).

Particle Measurements

Particle velocity and temperature are key factors affecting deposition efficiency, coating quality, and microstructure. This study used two measurement systems to monitor these parameters. The Cold Spray Meter (CSM) eVOLUTION by Tecnar Automation Inc. (Saint-Bruno-de-Montarville, Canada) measured particle velocity during CGS: a 790 nm, 3.3 W laser illuminates particles in the spray plume, and a sensor with an optical two-slit mask detects their velocity based on time-of-flight between slits. Due to limited powder, measurements were performed on 5,000 particles. The Accuraspray System (G3) from Tecnar was used to measure particle velocity and temperature during the HVAF process. Unlike methods using lasers, it employs CCD imaging and two-wavelength pyrometry based on Planck's law, assuming particles act as gray bodies. Only surface temperatures are measured, calculated from energy ratios at two wavelengths. Particle velocity measurement is similar to the Cold Spray Meter, analyzing optical signals from the plume. The Accuraspray G3 reports average values within a Ø 0.4 mm × 1.9 mm measurement volume and cannot assess individual particles. Its detection limit for temperatures is about 1000 °C due to weak thermal radiation from cooler particles.

Residual Stress Measurements

Residual stresses in coatings produced by various thermal spraying methods are measured using the incremental hole drilling technique. All substrates undergo laser texturing for consistent roughness, with identical preparation and coating thickness applied for comparison. For CGS and VPS, traditional treatments like grinding and polishing are also tested. In this method, incremental hole drilling disturbs mechanical equilibrium, causing measurable surface strain. Residual stress depth profiles are then calculated from these strains using Hooke's law. A drilling device, the RS-200 Milling Guide from Vishay Precision Group (Malvern, PA, USA), fitted with a TiN-coated end mill (Ø 1.6 mm), is used for the drilling process. The strain relaxations were measured using strain gauge rosettes (CEA-06-031-120 type from Micro-Measurements, Raleigh, NC, USA) applied to the surface at 0°, 45°, and 90° angles. The evaluation of the measurement results is carried out using the differential method (Ref 44), with a measurement accuracy of approximately 20 MPa. To calculate the residual stresses from the measured strain relaxations, the differential method is applied using the elastic constants E = 222885 MPa, v = 0,301 according to Kröner (Ref 45) based on single crystal coefficients from (Ref 46).

Adhesive Tensile Strength Measurements

A key parameter for evaluating thermally sprayed coatings is the adhesive tensile strength between the coating and substrate (DIN EN ISO 14916) (Ref 47). Initial experiments used the same substrate surface preparation for all processes, followed by additional tests with specific preparations for CGS and VPS. Coated round samples (Ø 25 mm x 3 mm) are bonded between metal cylinders/stamps (Ø 25 mm), with the stamp surfaces roughened by sandblasting (Al2O3, F36, 6 bar) before bonding. A new adhesive, Loctite 9658 (HTK Hamburg GmbH, Hamburg, Germany), is used as a replacement for the previously used FM1000 adhesive, which is no longer available. For the bonding, two adhesive films (approx. 600 µm) are applied to each side, as per the standard procedure. The samples are clamped in a holder, and adhesive is applied with screw pressure and cylindrical springs. For bonding, a torque wrench is used to apply a defined torque. The samples are then heat-treated in an oven at 177 °C ± 6 °C for two hours, as specified by the adhesive manufacturer. The adhesive's tensile strength is rated at 100 MPa. Three samples are tested per condition, and a dummy sample is prepared to check for potential variations, such as oven temperature inconsistencies. Tensile testing is performed using a type ZMART.PRO testing machine from Zwick

Roell (Ulm, Germany) at a constant test speed of 1 mm/s. After testing, the failure mode of the samples is analyzed. Four failure types are distinguished: adhesive failure (failure at the interface between substrate and coating), cohesive failure (failure within the coating), a combination of both, or adhesive failure due to weak bonding of the adhesive itself.

Results and Discussion

Comparison of Particle Temperature and Velocity

An initial analysis of particle states is conducted using the final process parameters for the three different thermal spray processes. Particle temperatures and velocities play a crucial role in determining the properties of the resulting coatings. Thermal and kinetic conditions vary significantly between methods, resulting in different coating formation mechanisms. The examination of particle states enables a deeper understanding of the interactions between process parameters and the resulting coating properties across different coating processes.

Figure 1 illustrates particle temperatures and velocities both qualitatively, through range indicators, and quantitatively, where measurement data are available. It becomes clear that HVAF achieves the highest average particle velocities of 920 m/s and, consequently, the highest kinetic energy. The average particle velocity for CGS is approximately 100 m/s lower than the HVAF process reported here. In contrast, VPS is expected to produce the lowest velocities. However, VPS is anticipated to achieve the highest average particle temperature and thus the highest level of thermal energy, even with the use of coarse powder (Ref 38). This high temperature is expected to lead to a complete melting of the particles. CGS, on the other hand, exhibits the lowest temperatures, as the gas temperature of 1100 °C results in particle temperatures well below this value, making particle melting unlikely. For HVAF, an average particle temperature of 1350 °C was measured, which is within the melting range of conventionally cast CMSX-4 (solidus temperature, T_s, 1330 °C, and liquidus temperature, T_l, 1396 °C (Ref 48)). This indicates that certain particles are either entirely molten or exhibit partial softening or melting.

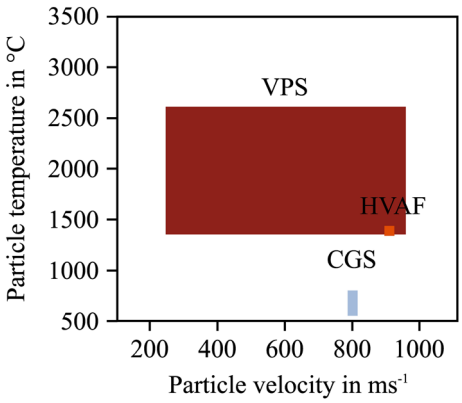

Fig. 1 Particle temperature and particle velocity for the three methods used (CGS, HVAF and VPS) with the CMSX-4 powders, (measured values are given precisely if available; otherwise, the temperature and velocity ranges are estimated)

Comparison of Single-Splat Experiments

The temperature and velocity analyses provide an initial comparison of the different methods. To gain further insights into particle states, additional single-splat analyses were conducted. These experiments enable a detailed investigation of individual particles upon impact with the substrate surface. Figure 2 shows BSE-SEM images of the single-splat sample surfaces for the three methods studied. At this point, it should be mentioned again that the fine powder was used for CGS and HVAF and the coarse powder for VPS. The particles in CGS (Fig. 2a)) exhibit limited macroscopic deformation, as a significant number of particles maintain a relatively spherical morphology with only localized flattening at the interface. This is consistent with the low particle temperatures, which inhibit melting or softening and thereby limit deformability. Additionally, morphological features indicative of material jetting are observed at the particle peripheries, suggesting the occurrence of adiabatic shear instabilities during impact. Furthermore, as documented in previous studies (Ref 42), craters are present on the sample surface, indicating that individual particles may fracture due to brittle TCP-phases within the material.

In contrast, few particles retain their original shape in the HVAF splats (Fig. 2b). The particles exhibit varying states post-coating. Many particles are partially molten, displaying fractured, rugged structures. These features are primarily attributed to mechanical fragmentation upon high-velocity impact, although localized thermal stress cracking due to rapid cooling may also contribute to the final morphology. In these splats, some portions of the material have melted, while others remain solid but softened. Fully molten splats are also visible, consistent with the measured particle surface temperatures. The varying state of the individual splats is partly attributed to differences in splat size, with smaller powder particles melting faster due to their lower mass.

The VPS sample (Fig. 2c) reveals that, due to significantly higher temperatures above the melting point, many splats are fully molten. This observation confirms that the high energy and sufficient particle residence time within

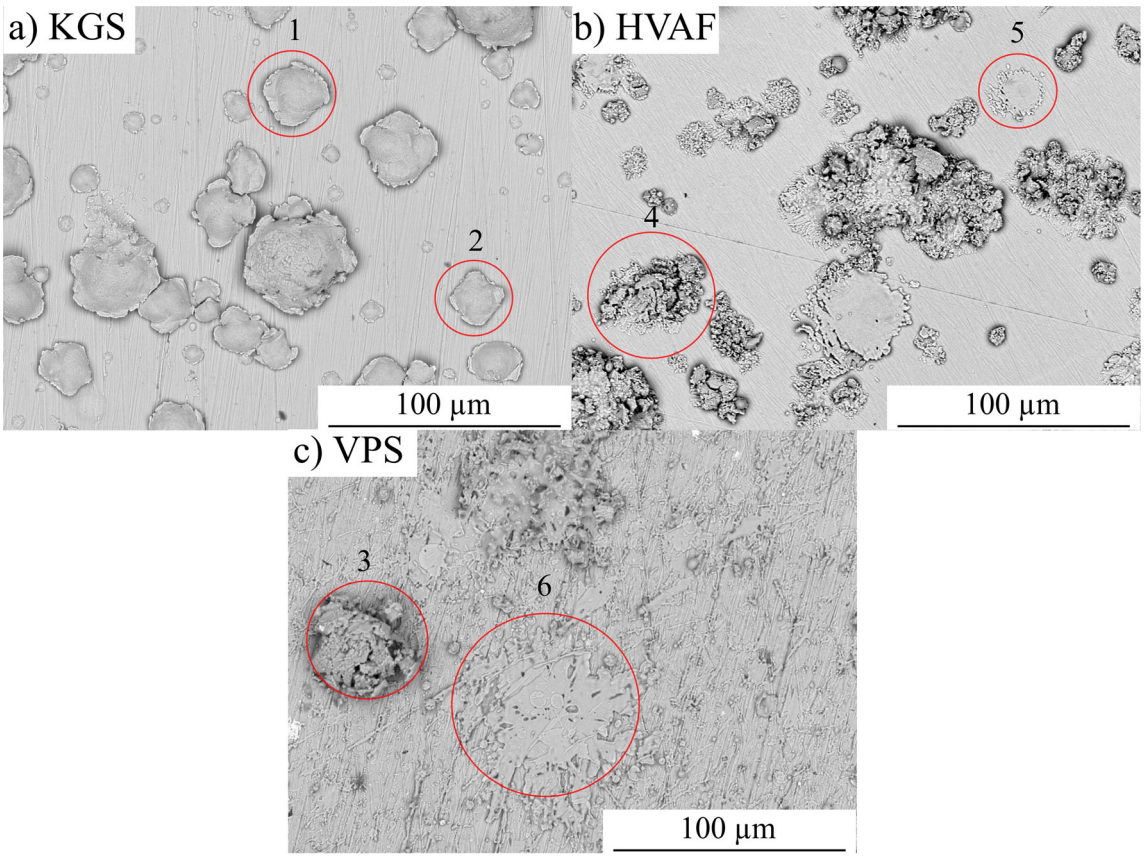

Fig. 2 Backscattered electron (BSE)-SEM images of the single-splat samples for the different methods (marked in red are the different particle states: 1&2 softened, 3&4 partially molten and 5&6 molten splats): (a) CGS, (b) HVAF and (c) VPS (Color figure online)

the plasma allowed the particles to achieve complete melting before impact. Some softened and partially molten particles are also present on the sample surface, indicating the natural variance in particle trajectory and residence time within the plasma flame. These particles missed the optimal high-temperature core of the plasma jet and thus received insufficient thermal energy for complete melting. The fully molten splats are noteworthy for their irregular shapes and fine splashed patterns, which is likely due to poor wetting as discussed in (Ref 38).

The varying splat states indicate expected differences in coating microstructures, which can substantially influence properties like porosity, adhesion, and residual stresses. For CGS and HVAF, compressive residual stresses are expected in the coatings since the particles impact in a solid state, contributing to peening effects. In contrast, tensile residual stresses are expected for VPS due to quenching stresses. Additionally, due to the partially molten particles and their structure in HVAF, a higher porosity is likely, as explained in the following section. Consequently, a detailed analysis of the microstructures is performed first.

Comparison of Microstructures

Overview images of cross sections from coatings produced by different methods are shown in Fig. 3(a), (c), and (e). It can be observed that coatings created with CGS and VPS exhibit slightly higher density compared to those produced by HVAF. Overall, all three coatings show a high density. The porosity values and oxygen content of the coatings are listed in Table 4. Notably, the oxygen content for the HVAF sample is derived from previous measurements conducted during process parameter optimization, as there was insufficient sample material available.

The lowest porosity is achieved by CGS ($0.6 \pm 0.1\%$) and VPS ($0.7 \pm 0.1\%$), while HVAF coatings show the highest porosity at $1.8 \pm 0.2\%$. VPS coatings attain their high density due to the high particle temperatures, which allow most particles to fully melt and deform more effectively. Additionally, the slow cooling rate, a result of the high temperature of the coating surface, enables particles to cool more gradually. This slow solidification allows particles and splats to adapt to the surface structure more closely, as the reduced viscosity facilitates better adhesion. The reason why HVAF coatings exhibit a more porous

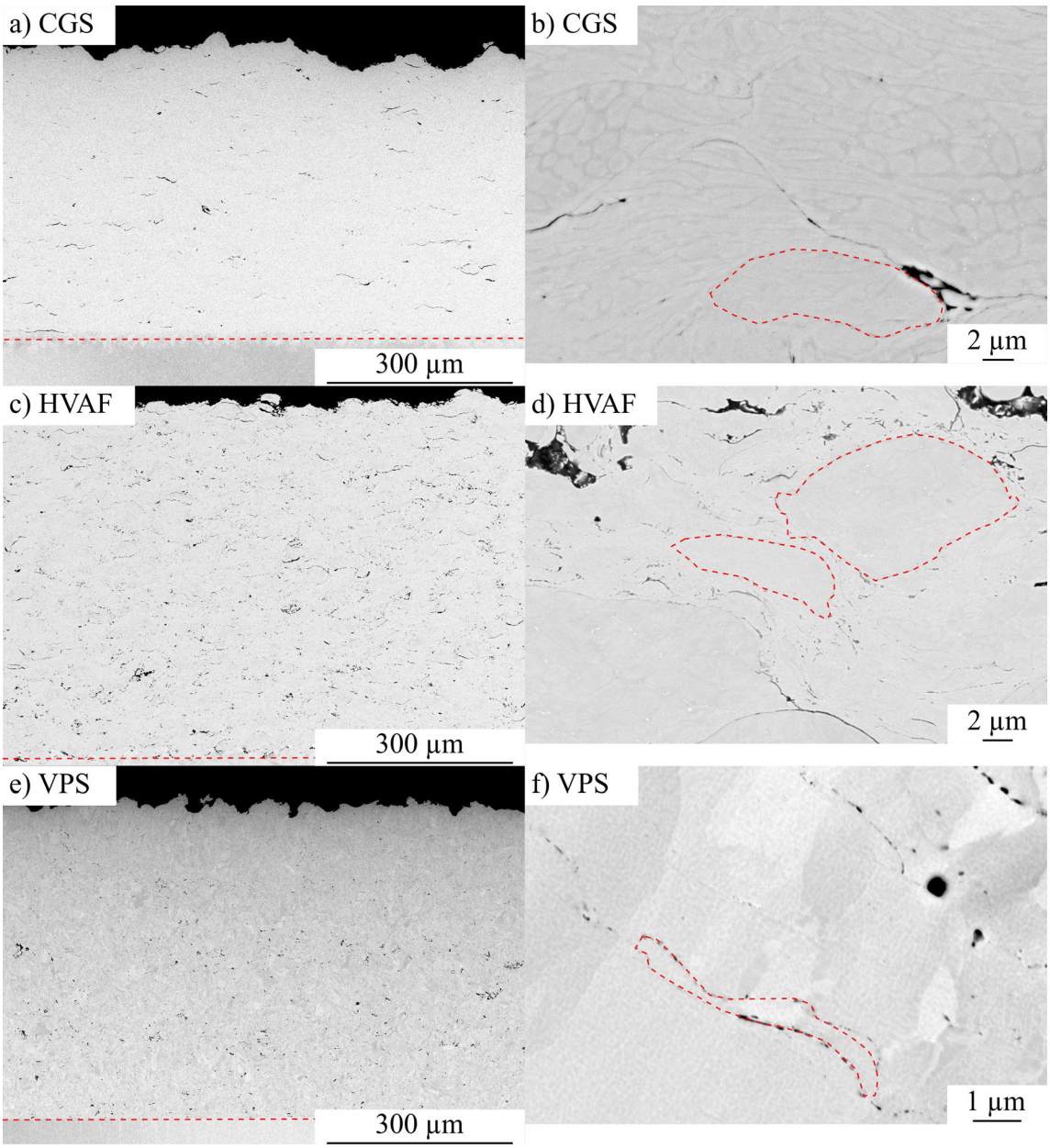

Fig. 3 BSE-SEM overview images of the coatings produced using different coating processes, with the interface between substrate and coating marked (red, dashed lines): **a** CGS, **c** HVAF, and **e** VPS. Additionally, BSE-SEM images of the coatings produced using different coating processes, taken at higher magnification, with individual splats marked (red, dashed lines): **b** CGS, **d** HVAF, and **f** VPS (Color figure online)

Table 4 Porosity and oxygen content of the coatings produced using different processes

Process	Porosity in %	Oxygen content in wt.%	Deposition efficiency in %
CGS	0.6 ± 0.1	0.073 ± 0.002	15.2
HVAF	1.8 ± 0.2	0.148 ± 0.014	34.2
VPS	0.7 ± 0.1	0.062 ± 0.008	49.1

structure, despite their higher particle temperatures and velocities compared to CGS coatings, can be explained through the single-splat analysis. In HVAF coatings, partially molten particles create a rugged structure upon impact, leading to a more irregular splat structure. Since the peening effect is likely reduced due to the softer particles, these semi-molten areas are not fully compacted by subsequent particles. In contrast, CGS particles retain their dense initial structure, as they are not softened or molten. Previous studies (Ref 42) have observed cracks within some CGS particles, which are likely closed as a result of the peening effect caused by subsequent particles. However, the lower (DE) suggests that a significant proportion of CGS particles may break off.

While higher temperatures generally promote oxidation kinetics, the final oxygen content in thermal spray coatings is ultimately controlled by the availability of oxygen (the process atmosphere). HVAF exhibits the highest oxygen uptake, which can be attributed to the process being carried out under standard atmospheric conditions at elevated temperatures. This oxygen-rich environment, combined with the higher porosity, allows more ambient oxygen to become trapped within the pores. CGS, which also operates under ambient conditions but at lower temperatures, shows a lower oxygen content at 0.073 ± 0.002 wt.%. Although the VPS plasma reaches the highest temperatures, the process is conducted under vacuum conditions. This lack of an oxidizing atmosphere is the dominant factor, resulting in a minimal oxidation. However, even with VPS, some oxygen uptake occurs, when compared to the powder feed stock (see Table 3).

Within the CGS-produced coatings, individual splats can be identified within the coating, a characteristic also observed to some extent in HVAF coatings. Figure 3(b) and (d) illustrates these particles, marked with red dashed lines. The visible particles in the HVAF coating are larger particles that did not completely melt due to relatively lower particle core temperatures. Conversely, splats of smaller, fully molten, or significantly deformed particles are more challenging to distinguish. The dendritic structure of the initial powder (Ref 42) is still fully preserved in CGS coatings and remains discernible in the larger particles of the HVAF coating. In VPS coatings, however, individual splats are difficult to identify. The dendritic solidification structure of the initial particles is no longer present, suggesting that the particles have undergone substantial melting. Instead, the coating exhibits a distinct grain structure, which will be discussed in more detail later. Compared to the other coatings, this one contains numerous fine, dark gray γ'-phases, as shown in Fig. 3(f). This is due to the high process temperatures, especially the elevated substrate and coating temperatures during coating (average substrate temperature: 1072 °C), which promote the precipitation and growth of the γ' phase. Literature suggests that accelerated γ' phase growth occurs at temperatures above approximately 800-900 °C (Ref 49, 50).

Impurity Phases in the Microstructure

This section presents a detailed analysis of impurity phases within the coatings. In all coatings, bright TCP phases are visible in the SEM images (see Fig. 4a, c, and e), which were already present in larger particles of the initial powder feed stock (Ref 42).

In the CGS coatings, no bright phases are observed in the smaller particles, consistent with the findings from the powder analysis. However, larger particles do show these bright precipitates. In the HVAF coating areas formed from molten particles, these phases are also absent. This absence may be due to the preferential melting of smaller particles that do not contain TCP phases. TCP phases in the hotter or molten particles dissolve at the elevated HVAF process temperatures, since these phases generally dissolve above 1100-1200 °C (Ref 51). Rapid cooling, when the particles impact the substrate, prevents re-precipitation of the TCP phases.

TCP phases are also present in the VPS coating. As an example, a larger TCP phase was analyzed using EDS (Fig. 4e and f). Increased concentrations of RE and W were detected, which typically occur in high proportions in these phases. As the areas are small, the surrounding microstructure is also detected, which rules out a quantitative analysis. It is evident that the VPS coatings exhibit a higher concentration of TCP phases in the regions adjacent to the substrate, as compared to the upper sections of the coating. This distribution is illustrated in Fig. 5.

In general, the TCP phases get completely dissolved due to the melting of most of the particles during the VPS process. However, the high coating temperatures during the process (average substrate temperature: 1072 °C) lead to the re-precipitation of these phases in the coating (Ref 51). The higher proportion of TCP phases in the lower coating area can be explained by the longer dwell times at higher temperatures, while the upper layer areas are only exposed to the higher temperatures for a shorter period of time. As a result, isolated large TCP phases are observed in the coating. Kalfhaus et al. (Ref 17) identified these phases as μ-type TCP phases, which form during solidification due to local chemical composition variations (Ref 52).

Pores and oxide fringes can be found between the individual splats in the CGS and HVAF coatings. The areas in which EDS measurements are carried out are shown in Fig. 4(a) and (c). It should also be noted that these are small areas so that the surrounding microstructure is also detected. At these locations, which appear darker in the BSE-SEM images, due to Z-contrast, increased oxygen and

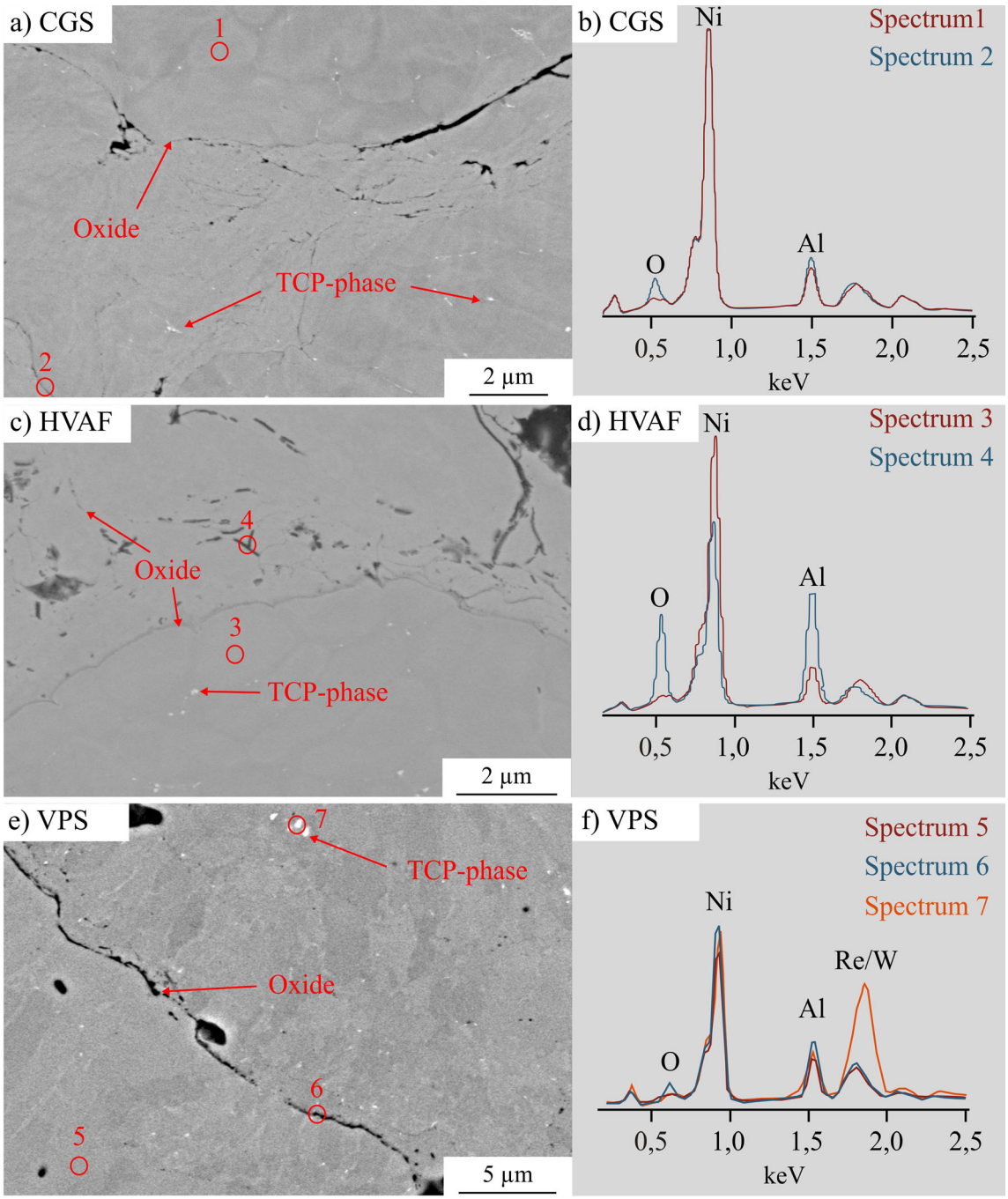

Fig. 4 BSE-SEM images of the coatings produced using different coating processes, with marked EDS analysis areas: (a) CGS, (c) HVAF, and (e) VPS, along with the corresponding spectra: (b) CGS, (d) HVAF, and (f) VPS

aluminum values can be detected (see Fig. 4b and d). This may indicate the presence of aluminum oxide. It is assumed that an oxide layer is formed around the particles during the coating process, especially during particle flight. In addition, oxidation of the substrate or coating surface may also occur. With the VPS coating, however, oxidation occurs between the individual coating layers (see Fig. 4e, f and 6.

This indicates that the main oxidation takes place between the individual coating cycles and not during the

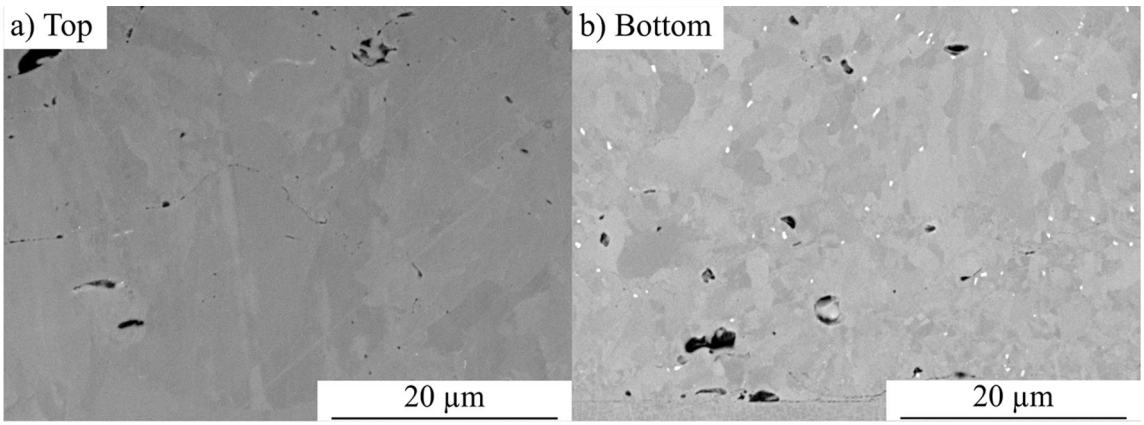

Fig. 5 BSE-SEM image of the TCP phases in the VPS coating: (a) at the coating surface and (b) at the interface to the substrate

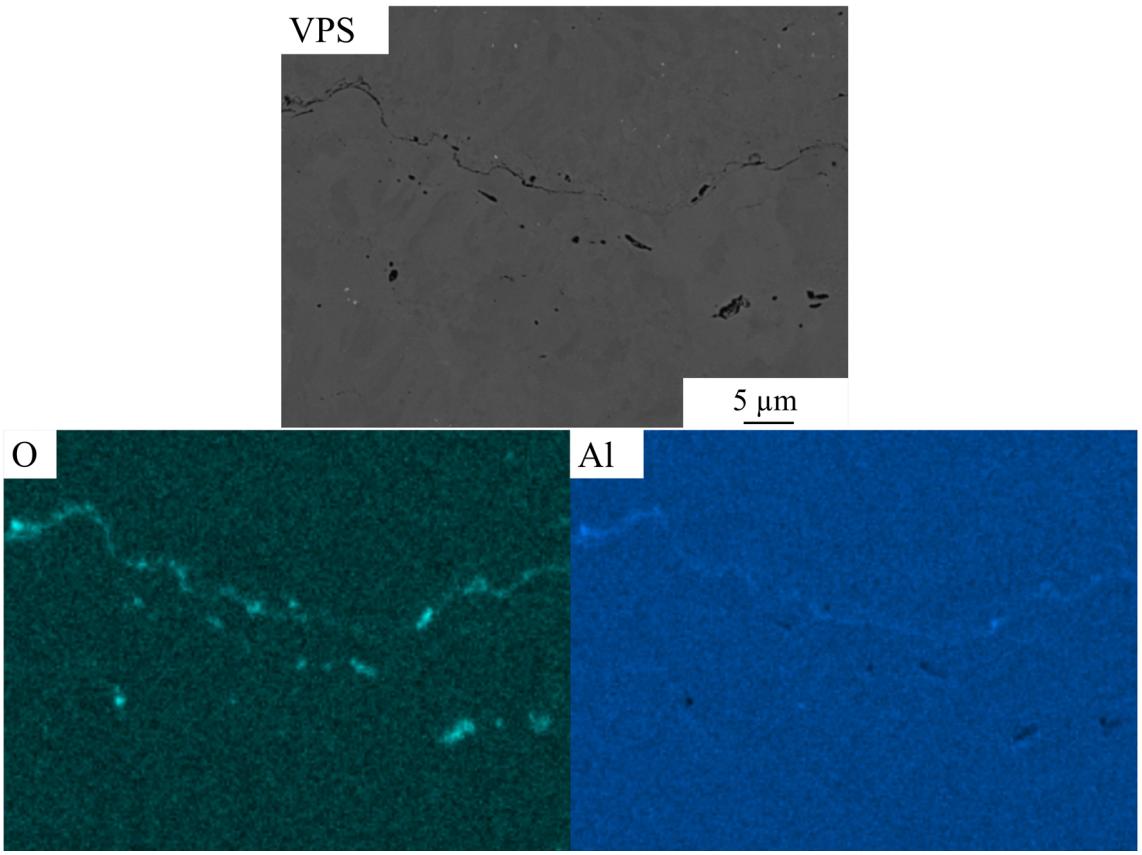

Fig. 6 EDS analysis between two layers of the VPS sample with the analyzed area and the element mappings for oxygen and aluminum

particle flight. This cannot be proven for the CGS and HVAF coatings, as the application per transition is too low and no individual layers are discernible.

Grain Structure of the Microstructure

The grain structure is particularly important for the subsequent planned directional recrystallization. It is necessary to have a fine microstructure, as this increases the driving force for grain growth. This is intended to subsequently convert the fine-grained microstructure into a columnar or single crystal microstructure. The grain structure of the coatings is influenced by the different processing conditions. For this reason, electron backscatter diffraction (EBSD) analyses were performed on the coatings. The EBSD data are presented in Fig. 7.

Notably, the color-coded IPF-Z map (building direction) of the CGS sample (Fig. 7a) shows many black regions.

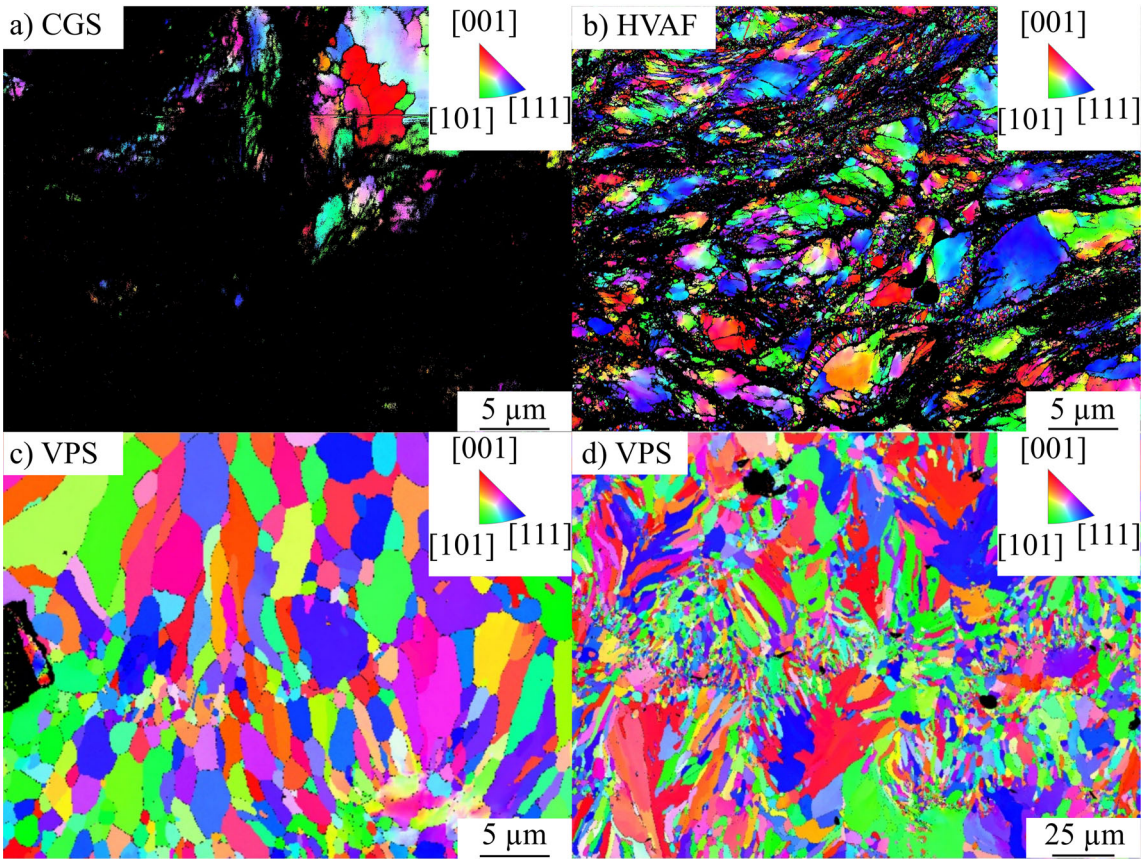

Fig. 7 Color-coded EBSD IPF-Z map: (a) CGS, (b) HVAF, (c) VPS and (d) VPS at a lower magnification

These are also present, though in much smaller quantities, in the HVAF sample (Fig. 7b). These areas can be explained by the coating formation processes of the two methods. The solid particles are primarily deformed at the edges, while the core remains largely unchanged. There are two possible reasons for the lack of signal in the highly deformed regions. First, dynamic recrystallization may have occurred as a result of severe plastic deformation (Ref 53). Dynamic recrystallization can lead to the formation of a fine nanocrystalline structure, with grain sizes falling below the step size and resolution limits of the EBSD detector. Second, the high dislocation density in these areas could significantly hinder EBSD detection. The IPF map of the samples shows a random texture, i.e., no preferred orientation of the grains. For HVAF, it is also possible that the rapid cooling of the molten and semi-molten particles on the substrate contributes to the fine structure. Additionally, both coatings exhibit low-angle grain boundaries, which could originate from deformation during the deposition process. This is supported by the observation of gradual orientation changes within individual grains in the IPF maps. The VPS coating (Fig. 7c, d) exhibits a columnar or column-like grain structure in certain areas, as reported by Kalfhaus et al. (Ref 17). The grain sizes in the coating vary significantly, as shown in Fig. 7(d). It is assumed that the columnar grain morphology is caused by directional heat dissipation through the substrate, but the overall texture is weak due to the random orientation of individual splats and the overlapping growth of multiple deposition layers.

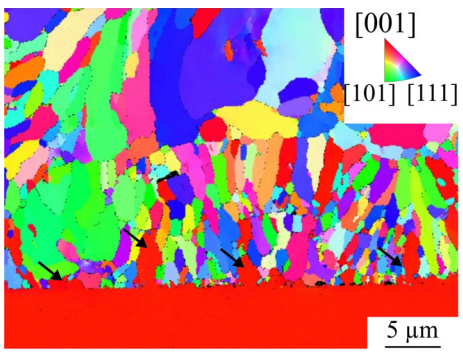

Fig. 8 Color-coded EBSD-IPF-Z map of the VPS interface, black arrows indicate epitaxially grown grains

Figure 8 shows the interface between the coating and the substrate for the VPS coating. As reported by Kalfhaus et al. (Ref 17), epitaxial growth occurs in certain areas due to the high substrate temperature. The red color of the

substrate confirms the [001] orientation of the single-crystal substrate. Epitaxially grown grains can be identified in the IPF-Z map of the sample by the same color. Some of these grains extend several micrometers (up to 5 µm) into the coating. It is assumed that these grains have grown over multiple splats. Such epitaxial growth can enhance adhesion to the substrate by providing a continuous crystallographic interface with fewer high-angle grain boundaries, thereby improving, for example, load transfer and reducing potential crack initiation sites. This demonstrates that plasma preheating can achieve microstructures (porosity, oxygen content, epitaxial areas) comparable to substrate heater preheating, as used by Kalfhaus et al. (Ref 17).

Comparison of Residual Stresses

This section provides a detailed investigation of the residual stress states in the coatings using the incremental hole-drilling method. The investigation of residual stresses is crucial, as the stresses can contribute significantly to the formation of cracks or delamination of the coatings. The residual stress states in the coating systems differ, due to the different processing conditions, such as particle states and coating process. To ensure better comparability of the results an identical substrate pre-treatment was applied for all processes. Since laser texturing was identified in previous studies as the only viable pre-treatment for HVAF, this pre-treatment was also applied for the other processes. Additionally, the commonly used substrate pre-treatments for CGS (grinding) and VPS (polishing) were examined to enable a comprehensive comparison.

Figure 9 illustrates the residual stress profiles over the coating thickness for the different processes, derived from the measured strain relaxations. It is important to note that the stress values near the surface are subject to uncertainties due to the pronounced surface topography of the sprayed coatings. In general, it can be observed that the profiles of the two stresses (σ_a and σ_c) align well, indicating an axisymmetric in-plane stress state. Both the CGS and HVAF coatings exhibit compressive residual stresses, which can be explained as follows. In the CGS process, there are typically no molten particles. Moreover, the results from single-splat analyses revealed that in HVAF, only a few particles are fully molten. Thus, in contrast to the high-temperature thermal spraying processes, quenching stresses—which would result in tensile residual stresses—are not predominantly expected. Instead, in both processes, the relatively solid particles impact the surface at high velocity, resulting in high kinetic energy. This leads to plastic deformation, generating in-plane compressive residual stresses within the coating (Ref 54, 55). The highest compressive residual stresses are found in the near-surface region, which decrease across the coating thickness and are eventually balanced by tensile residual stresses. The reason for this trend might be explained by the dynamic bending of the sample during the continuous coating process. The curvature increases with each applied layer, which further deforms the existing layers (Ref 56). This deformation leads to lower compressive residual stresses in the deeper layers, thus causing the observed increase in surface stress. Additionally, the manner in which the sample is clamped may also influence the outcome. This effect is expected to be less pronounced, with increasing substrates thickness. However, it is clear that compressive residual stresses are present in both kinetic processes. Despite a slight deformation of the samples, the results remain comparable and reflect conditions that are also present in a real-world application. Consequently, the measured residual stress as a function of depth represents a crucial process parameter, as it provides valuable insight into the evolution of residual stress profiles under these specific conditions. The HVAF coating exhibits compressive residual stresses of approximately 500–600 MPa, which are higher than those observed in the CGS coatings, measured at around 400 MPa. A possible reason for this is the higher average particle velocity achieved in HVAF. This higher velocity leads to increased kinetic energy of the particles, which, in turn, results in higher compressive residual stresses in the coating (Ref 57, 58). However, the particle temperature is also higher in the HVAF process, which leads to greater deformability of the impacting particles and, thus, might diminish the peening effect, and therefore the compressive residual stresses in the coating. Additionally, dynamic recrystallization may also play a role in reducing residual stresses in both processes, although this effect is likely more pronounced in HVAF due to its higher overall temperatures. Therefore, higher compressive residual stresses would be expected for CGS. It is likely that, as discussed in in a previous paper (Ref 42), crack formation in the brittle powder and the chipping off from many particles in the CGS process leads to a release of the stresses. This is underscored by the low DE observed for the CGS.

In contrast, the VPS coatings show a near stress-free state with a slight amount of tensile residual stresses. Typically, tensile residual stresses arise in coatings from thermal spraying processes due to quenching of the individual splats on the cold substrate. Owing to the elevated average substrate and coating temperatures, which exceed 1000 °C, the cooling rate is comparatively slow. These high temperatures enable partial relaxation of residual stresses, resulting in the coating being either nearly stress-free or experiencing only minimal tensile residual stress. At the process temperature of approximately 1072 °C, the yield strength of CMSX-4 decreases considerably, allowing for immediate plastic deformation that alleviates

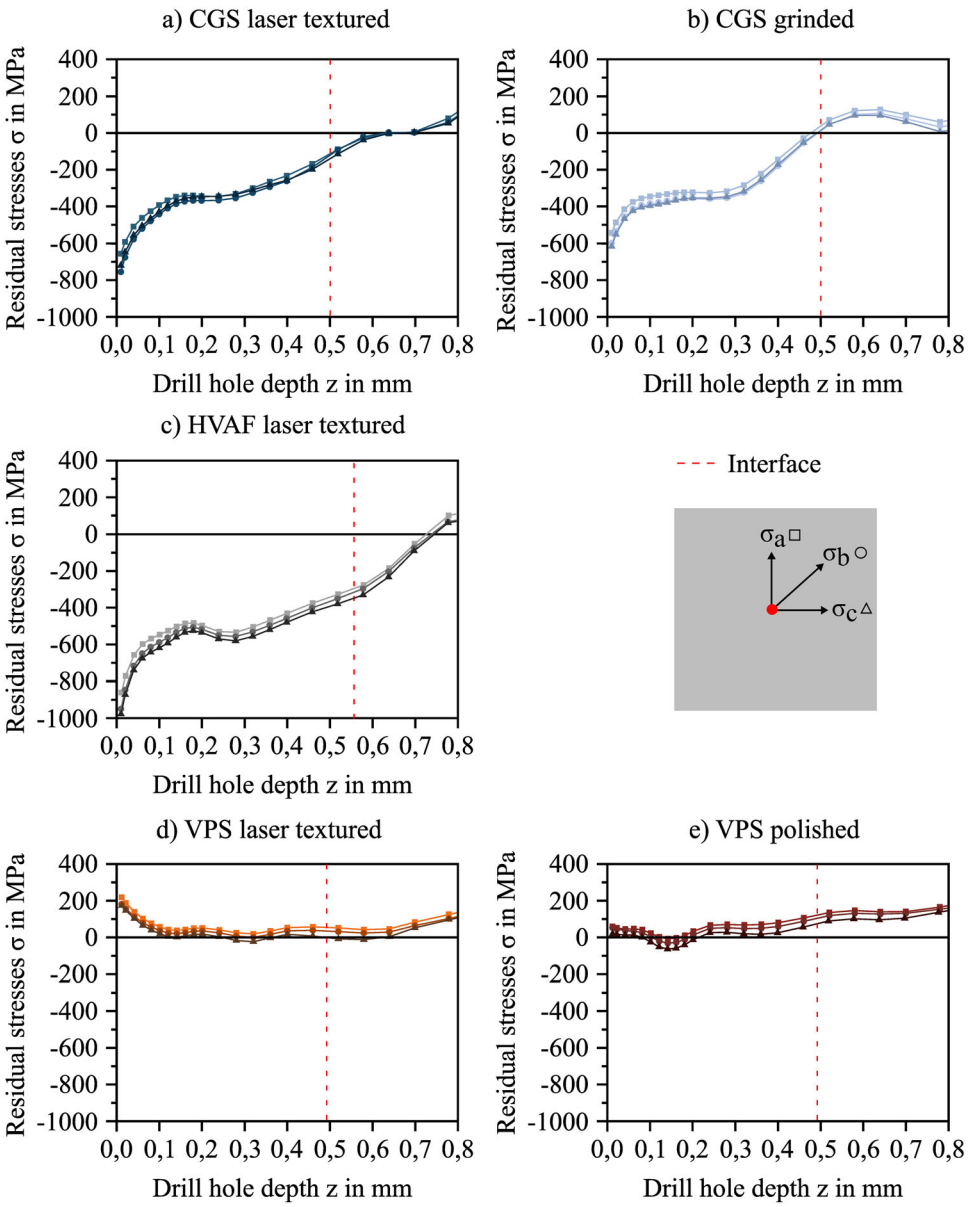

Fig. 9 Residual stress depth curves determined using the incremental hole drilling method: (a) CGS laser textured, (b) CGS grinded, (c) HVAF laser textured, (d) VPS laser textured and (e) VPS polished

quenching-induced stresses. The substantial atomic mobility at this temperature is further demonstrated by the epitaxial growth present at the coating–substrate interface, as noted in the microstructural analysis. This observation suggests that diffusion processes are sufficiently rapid to permit atoms to align into a low-energy, coherent lattice, thereby preventing significant accumulation of residual stresses. There is no significant difference observed for the surface pre-treatments in CGS and VPS.

Comparison of Adhesion Strength

This section discusses the results of the adhesion strength of the coatings. As previously mentioned in relation to the residual stress analyses, the same substrate pre-treatment was applied to all coatings. Furthermore, the specific substrate preparations for CGS and VPS were also investigated. Figure 10(a) shows the average adhesion strength measured on three samples each. Initially, the dummy samples reveal that the adhesion strength specified by the manufacturer as 100 MPa was not achieved. This could possibly be due to insufficient heating rates, which may have caused premature curing of the adhesive. The dummy experiments also show a deviation of approximately 20 MPa. This discrepancy can thus be treated as the experimental error between measurements. Potential effects on tensile adhesion results can arise from slight sample curvatures, which cause a non-uniform adhesive

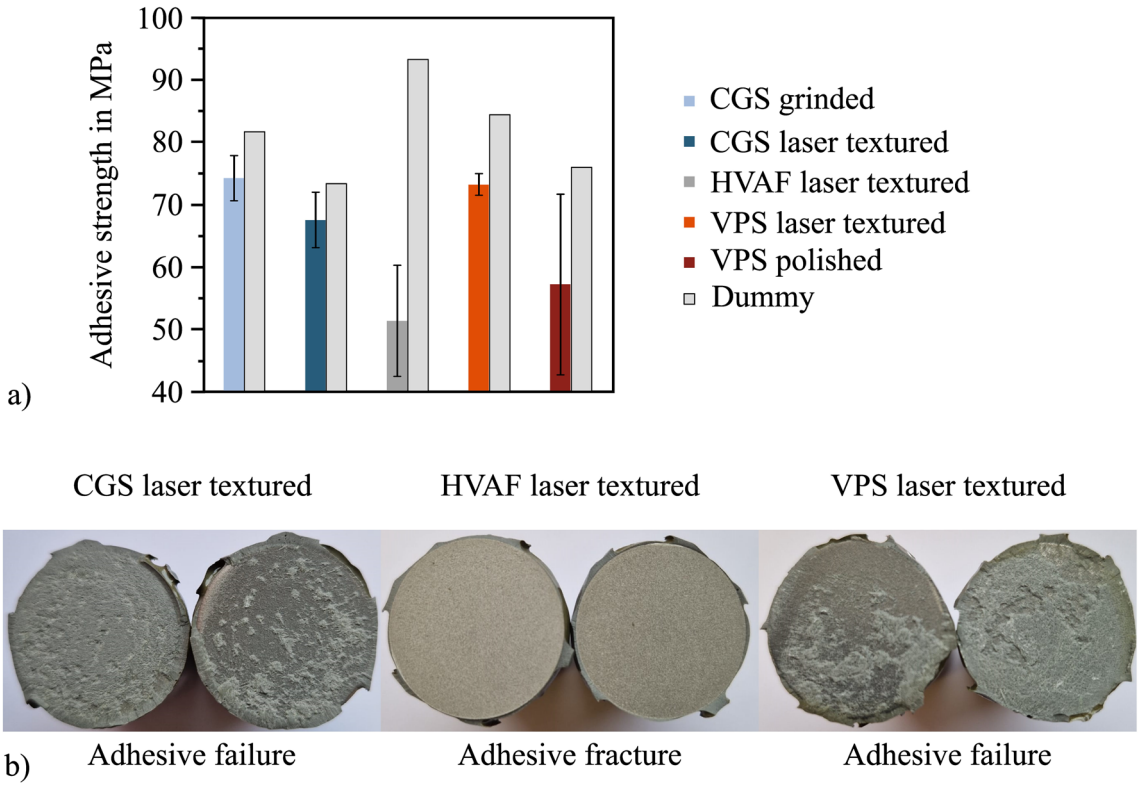

Fig. 10 (a) Adhesive strengths of the coatings produced by CGS (polished and laser textured), HVAF (laser textured), and VPS (polished and laser textured), additionally the respective dummy samples of the individual test runs are shown on the right in light gray, which serve as reference values and (b) the exemplary stamp surfaces of the different tests, which show the different types of failure

bond line. This inconsistency in the bond can compromise the integrity of the adhesion and consequently lead to skewed tensile test values.

By comparing the adhesion strengths of the different processes using the same substrate pre-treatment, it is evident that adhesive failure occurred (Fig. 10b) in both the CGS and VPS samples, as their adhesion strengths surpassed that of the adhesive. Therefore, no conclusion can be drawn regarding which of the two processes exhibits higher adhesive fracture. Only the HVAF samples showed significantly lower adhesion strength, with an adhesion failure occurring at the interface between the substrate and the coating. This can be explained by the higher level of compressive residual stresses in the HVAF coating observed from the incremental hole-drilling method, which indicates a higher level of stored elastic energy in the HVAF coating. When the critical energy release rate of the interface is exceeded, delamination occurs.

A comparison of the two pre-treatment methods for CGS reveals nearly identical adhesion strengths, both resulted in adhesive failure. Therefore, it is not possible to draw any conclusions regarding the impact of the substrate pre-treatment on the outcome. In contrast, the adhesion tests on the polished VPS samples revealed a wide variation in the results, as indicated by the large error bar. Two samples showed adhesive failure, with one already failing at approximately 55 MPa.

The dummy sample in this series showed an adhesion strength of 76 MPa, which was also reached by the second sample with adhesive failure. One possible cause for these deviations could be the non-coaxial bonding of the stamps, leading to an uneven load distribution. The third sample in this series showed an adhesion failure between the coating and the substrate, resulting in an adhesion strength of only 40.8 MPa. A closer examination of the fracture surface (see Fig. 11b) indicates that adhesive likely penetrated between the coating and the substrate. Since the sample holder in the VPS test applies force from the side, partial detachment of the coating may occur when releasing the samples from the holding jaws, as visible in Fig. 11(a).

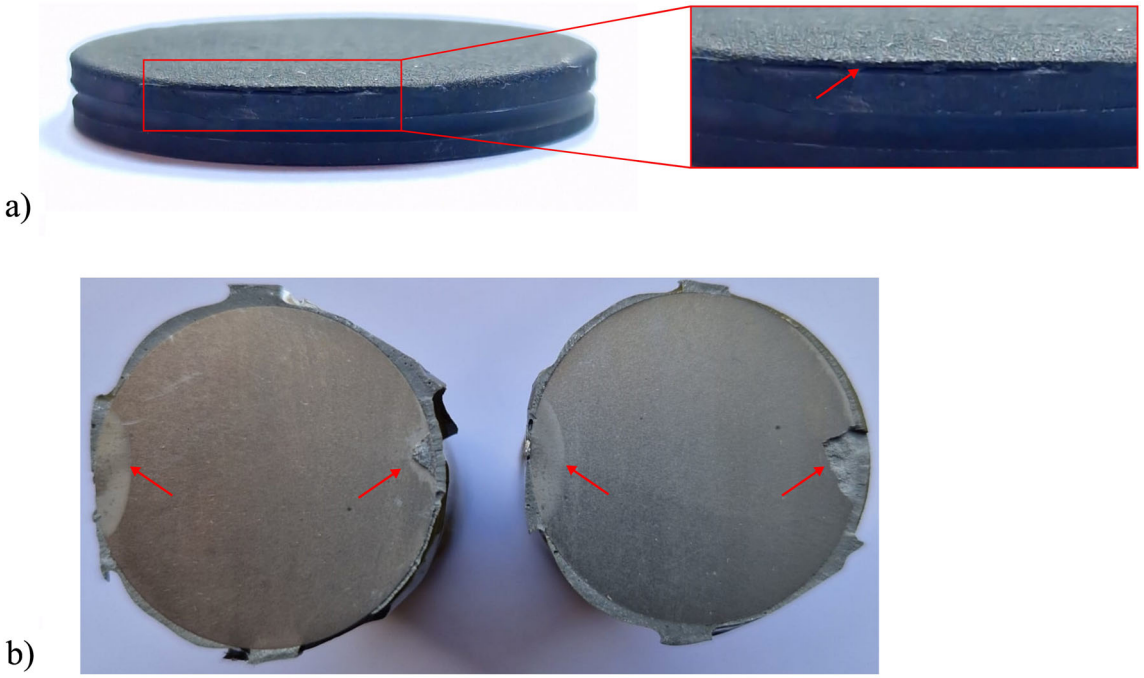

Fig. 11 (a) Coated VPS adhesive tensile test specimen with detached layer in the area where the specimen is clamped during the coating process and (b) VPS specimen after the adhesive tensile test with an adhesion fracture and the areas where the adhesive has run between the layer and substrate marked with red arrows (Color figure online)

This leads to the adhesive running between the coating and the substrate during the bonding of the sample with the stamps, which can weaken the adhesion.

These results are also reflected in the trial where 2 mm thick coatings were produced using different processes. For the HVAF coatings, delamination during spraying occurred when a coating thickness of approximately 1.2 mm was achieved. The CGS coating delaminated after reaching a thickness of about 1.5 mm. Only with VPS was it possible to produce 2 mm thick coatings. The underlying reason is that an increase in coating thickness leads to an increased level of stored elastic energy. This energy eventually causes delamination once the interfacial strength is surpassed.

The reason for the delamination in the HVAF coatings is likely due to the highest compressive residual stresses present in these coatings during deposition, which led to the earliest failure. In contrast, for CGS, it can be assumed, based on the low deposition efficiency and findings from paper (Ref 42), that continuous stress relaxation occurs during the coating process. This results in the detachment of particle fragments early on. Eventually, the remaining coating exceeds the critical energy release rate and delaminates as well. Additionally, dynamic recrystallization may contribute to a reduction of residual stress levels, and therefore a better adhesion. On the other hand, as VPS coatings are almost entirely free of residual stresses, the stored elastic energy is minimal, making it the most stable in terms of coating thickness. Moreover, by seamlessly extending the substrate's crystal lattice, epitaxially grown grains improve thermal spray adhesion by forming a strong metallurgical bond and reducing defects at the interface.

Conclusion and Outlook

This study presents a comprehensive comparison of three thermal spray coating processes—CGS, HVAF, and VPS—evaluating their suitability for repair applications. The investigation focused on particle characteristics, microstructural properties, and mechanical performance. The conclusions presented here are most directly applicable to the specific process parameters and geometric conditions of this study, including the 3 mm thick substrates and coating thicknesses of approximately 500 µm.

Analysis of particle states revealed distinct process conditions. HVAF achieved the highest particle velocities, while VPS produced the highest temperatures leading to complete particle melting. CGS maintained the lowest particle temperatures without melting. These variations were evident in single-splat experiments, where CGS particles largely retained their initial compact form and deformed into flattened, disk-shaped particles upon impact, HVAF particles showed mixed states, and VPS produced fully molten splats with fine spatters.

Microstructural analysis demonstrated lowest porosity values (0.6-0.7 %) for CGS and VPS, while HVAF exhibited 1.8 % porosity. All coating variants contained aluminum oxides, with VPS showing lowest oxygen content due to vacuum conditions; moreover, the oxides in VPS were found between the coating layers. EBSD analysis revealed nanocrystalline regions in CGS and HVAF coatings, while VPS coatings displayed columnar grain structures with epitaxial growth at the substrate interface.

Regarding residual stress states for the given test setup, CGS and HVAF coatings revealed compressive residual stresses due to peening effects, while VPS coatings remained nearly stress-free. Adhesion strength testing showed superior performance for CGS and VPS coatings, when compared to HVAF. Thickness limitations became apparent in 2 mm coating attempts, with HVAF and CGS experiencing delamination at 1.2 mm and 1.5 mm respectively, while VPS successfully achieved 2 mm thickness under the given conditions. The findings suggest that VPS may be the most suitable process for larger area repairs, as other methods could lead to premature coating delamination. However, the inhomogeneous grain size distribution, especially the presence of larger grains, could pose a significant challenge for the planned directional recrystallizations, as a finer microstructure provides a higher driving force for grain growth.

Funding Open Access funding enabled and organized by Projekt DEAL.

References

1. S. Ackert, Basics of Aircraft Maintenance Reserve Development and Management, Aircraft Monitor, 2012.
2. R.C. Reed, *The Superalloys: Fundamentals and Applications*, Cambridge University Press, Cambridge, 2006.
3. D. Goldschmidt, Einkristalline Gasturbinenschaufeln aus Nickelbasis-Legierungen. Teil I: Herstellung und Mikrogefüge (Single-Crystal Gas Turbine Blades Made of Nickel-Based Alloys. Part I: Manufacture and Microstructure), *Mat.-wiss. u. Werkstofftech.*, 1994, **25**, p 311–320.
4. A. Basak, R. Acharya, and S. Das, Additive Manufacturing of Single-Crystal Superalloy CMSX-4 Through Scanning Laser Epitaxy: Computational Modeling, Experimental Process Development, and Process Parameter Optimization, *Metall. Mater. Trans. A*, 2016, **47**(8), p 3845–3859. https://doi.org/10.1007/s11661-016-3571-y
5. J.M. Wilson, C. Piya, Y.C. Shin, F. Zhao, and K. Ramani, Remanufacturing of Turbine Blades by Laser Direct Deposition with its Energy and Environmental Impact Analysis, *J. Clean. Prod.*, 2014, **80**, p 170–178. https://doi.org/10.1016/j.jclepro.2014.05.084.
6. A. Aprilia, W. L. K. Nguyen, A. Khairyanto, W. C. Pang, S. B. Tor, G. Seet, Towards automated remanufacturing process with additive manufacturing
7. R.M. Macintyre, The use of lasers in Rolls-Royce, *Laser Surface Treatment of Metals*. C.W. Draper, P. Mazzoldi Ed., Springer Netherlands, Dordrecht, 1986, p 545–549. https://doi.org/10.1007/978-94-009-4468-8_47
8. Q.-L. Zhang, J.-H. Yao, and J. Mazumder, Laser Direct Metal Deposition Technology and Microstructure and Composition Segregation of Inconel 718 Superalloy, *J. Iron. Steel Res. Int.*, 2011, **18**(4), p 73–78. https://doi.org/10.1016/S1006-706X(11)60054-X
9. H. Qi, M. Azer, and A. Ritter, Studies of Standard Heat Treatment Effects on Microstructure and Mechanical Properties of Laser Net Shape Manufactured INCONEL 718, *Metall. Mater. Trans. A*, 2009, **40**(10), p 2410–2422. https://doi.org/10.1007/s11661-009-9949-3
10. B. A. Rottwinkel, Verfahrenstechnische Grundlagen für das epitaxiale Rissschweißen in einkristallinen Nickelbasis-Superlegierungen, Ph.D. thesis, MyCoRe Community, 2022, https://doi.org/10.21268/20221111-0
11. M. Gäumann, S. Henry, F. Cléton, J.-D. Wagnière, and W. Kurz, Epitaxial Laser Metal Forming: Analysis of Microstructure Formation, *Mater. Sci. Eng. A*, 1999, **271**(1–2), p 232–241. https://doi.org/10.1016/S0921-5093(99)00202-6
12. M. Gäumann, C. Bezençon, P. Canalis, and W. Kurz, Single-Crystal Laser Deposition of Superalloys: Processing–Microstructure Maps, *Acta Mater.*, 2001, **49**(6), p 1051–1062. https://doi.org/10.1016/S1359-6454(00)00367-0
13. R. Vilar, A. Almeida, and E.C. Santos, Multilayer Laser-Assisted Deposition on Single Crystal Superalloy Substrates, *Int. J. Microstruct. Mater. Prop.*, 2013, **8**(1/2), 4. https://doi.org/10.1504/IJMMP.2013.052642
14. R. Vilar and A. Almeida, Repair and Manufacturing of Single Crystal Ni-Based Superalloys Components by Laser Powder Deposition—a Review, *J. Laser Appl.*, 2015, **27**(S1), S17004. https://doi.org/10.2351/1.4862697
15. Z. Chen, W. Li, L. Wang, X. Wei, and Z. Liu, Investigation on the Hot Crack Sensitivity of a Nickel-Based Single Crystal Superalloy Fabricated by Epitaxial Laser Metal Forming, *J. Alloys Compd.*, 2023, **931**, 167436. https://doi.org/10.1016/j.jallcom.2022.167436
16. T.A. Owoseni, I. Ciudad De Lara, S. Mathiyalagan, S. Björklund, and S. Joshi, Microstructure and Tribological Performance of HVAF-Sprayed Ti-6Al-4V Coatings, *Coatings*, 2023, **13**(11), 1952. https://doi.org/10.3390/coatings13111952
17. T. Kalfhaus, M. Schneider, B. Ruttert, D. Sebold, T. Hammerschmidt, J. Frenzel, R. Drautz, W. Theisen, G. Eggeler, O. Guillon, and R. Vassen, Repair of Ni-Based Single-Crystal Superalloys Using Vacuum Plasma Spray, *Mater. Des.*, 2019, **168**, 107656. https://doi.org/10.1016/j.matdes.2019.107656
18. V. Champagne and D. Helfritch, Critical Assessment 11: Structural Repairs by Cold Spray, *Mater. Sci. Technol.*, 2015, **31**(6), p 627–634. https://doi.org/10.1179/1743284714Y.0000000723

19. T. Kalfhaus, H. Schaar, F. Thaler, B. Ruttert, D. Sebold, J. Frenzel, I. Steinbach, W. Theisen, O. Guillon, T. Clyne, and R. Vassen, Path to Single-Crystalline Repair and Manufacture of Ni-Based Superalloy Using Directional Annealing, *Surf. Coat. Technol.*, 2021, **405**, 126494. https://doi.org/10.1016/j.surfcoat.2020.126494
20. J. Fiebig, E. Bakan, T. Kalfhaus, G. Mauer, O. Guillon, and R. Vaßen, Thermal Spray Processes for the Repair of Gas Turbine Components, *Adv. Eng. Mater.*, 2020, **22**(6), 1901237. https://doi.org/10.1002/adem.201901237
21. J.W. Murray, M.V. Zuccoli, and T. Hussain, Heat Treatment of Cold-Sprayed C355Al for Repair: Microstructure and Mechanical Properties, *J. Therm. Spray Technol.*, 2018, **27**(1–2), p 159–168. https://doi.org/10.1007/s11666-017-0665-z
22. W. Li, K. Yang, S. Yin, X. Yang, Y. Xu, and R. Lupoi, Solid-State Additive Manufacturing and Repairing by Cold Spraying: A Review, *J. Mater. Sci. Technol.*, 2018, **34**(3), p 440–457. https://doi.org/10.1016/j.jmst.2017.09.015
23. David Edwin Budinger, Method for hvof or lpps restoration coating repair of a nickel-base superalloy, 2010
24. M. Minor, Turbine Component Crack Pepair using Cathodic Arc and/or Low Pressure Plasma Spraying and HIP, 2007
25. T. Schmidt, H. Assadi, F. Gärtner, H. Richter, T. Stoltenhoff, H. Kreye, and T. Klassen, From Particle Acceleration to Impact and Bonding in Cold Spraying, *J. Therm. Spray Technol.*, 2009, **18**(5–6), p 794. https://doi.org/10.1007/s11666-009-9357-7
26. S. Yin, P. Cavaliere, B. Aldwell, R. Jenkins, H. Liao, W. Li, and R. Lupoi, Cold Spray Additive Manufacturing and Repair: Fundamentals and Applications, *Addit. Manuf.*, 2018, **2**, p 628–650. https://doi.org/10.1016/j.addma.2018.04.017
27. R. Raoelison, Y. Xie, T. Sapanathan, M. Planche, R. Kromer, S. Costil, and C. Langlade, Cold Gas Dynamic Spray Technology: A Comprehensive Review of Processing Conditions for Various Technological Developments Till to Date, *Addit. Manuf.*, 2018, **19**, p 134–159. https://doi.org/10.1016/j.addma.2017.07.001
28. C.A. Widener, M.J. Carter, O.C. Ozdemir, R.H. Hrabe, B. Hoiland, T.E. Stamey, V.K. Champagne, and T.J. Eden, Application of High-Pressure Cold Spray for an Internal Bore Repair of a Navy Valve Actuator, *J. Therm. Spray Technol.*, 2016, **25**(1–2), p 193–201. https://doi.org/10.1007/s11666-015-0366-4
29. R.C. Tucker and R.C. Tucker Eds., *ASM Handbook. 5A: Thermal Spray Technology*, ASM International, Materials Park, Ohio, 2013
30. P. Khamsepour, J. Oberste-Berghaus, M. Aghasibeig, F.B. Ettouil, A. Dolatabadi, and C. Moreau, The Effect of Spraying Parameters of the Inner-Diameter High- Velocity Air–Fuel (ID-HVAF) Torch on Characteristics of Ti-6Al-4V In-flight Particles and Coatings Formed at Short Spraying Distances, *J. Therm. Spray Technol.*, 2023, **32**(2–3), p 568–585. https://doi.org/10.1007/s11666-023-01535-z
31. C. Yang and I. Baker, Directional Recrystallisation Processing: a Review, *Int. Mater. Rev.*, 2021han, **66**(4), p 256–286.
32. Z. Zhang, G. Chen, and G. Chen, The Effect of Drawing Velocity and Phase Transformation on the Structure of Directionally Annealed Iron, *Mater. Sci. Eng. A*, 2006, **434**(1–2), p 58–62. https://doi.org/10.1080/09506608.2020.1819688
33. I. Baker and J. Li, Directional Annealing of Cold-Rolled Copper Single Crystals, *Acta Mater.*, 2002, **50**(4), p 805–813. https://doi.org/10.1016/S1359-6454(01)00384-6
34. T. Clyne, Residual Stresses in Surface Coatings and Their Effects on Interfacial Debonding, *Key Eng. Mater.*, 1995 https://doi.org/10.4028/www.scientific.net/KEM.116-117.307
35. A.G. Evans, G.B. Crumley, and R.E. Demaray, On the Mechanical Behavior of Brittle Coatings and Layers, *Oxid. Met.*, 1983, **20**(5–6), p 193–216. https://doi.org/10.1007/BF00656841
36. T.W. Clyne and S.C. Gill, Residual Stresses in Thermal Spray Coatings and Their Effect on Interfacial Adhesion: A Review of Recent Work, *J. Therm. Spray Technol.*, 1996, **5**(4), p 401–418. https://doi.org/10.1007/BF02645271
37. S. Kuroda and T. Clyne, The Quenching Stress in Thermally Sprayed Coatings, *Thin Solid Films*, 1991, **200**(1), p 49–66. https://doi.org/10.1016/0040-6090(91)90029-W
38. P.L. Fauchais, J.V. Heberlein, and M.I. Boulos, *Thermal Spray Fundamentals: From Powder to Part*, Springer US, Boston, MA, 2014. https://doi.org/10.1007/978-0-387-68991-3
39. T. Varis, T. Suhonen, J. Laakso, M. Jokipii, and P. Vuoristo, Evaluation of Residual Stresses and Their Influence on Cavitation Erosion Resistance of High Kinetic HVOF and HVAF-Sprayed WC-CoCr Coatings, *J. Therm. Spray Technol.*, 2020, **29**(6), p 1365–1381. https://doi.org/10.1007/s11666-020-01037-2
40. J. Schmitt, J. Fiebig, S. Schrüfer, O. Guillon, and R. Vaßen, Adjusting Residual Stresses During Cold Spray Deposition of IN718, *J. Therm. Spray Technol.*, 2024, **33**(1), p 210–220. https://doi.org/10.1007/s11666-023-01673-4
41. ASTM E837-20, Standard Test Method for Determining Residual Stresses by the Hole-Drilling Strain-Gage Method. https://doi.org/10.1520/E0837-20
42. M. Létang, J. Schmitt, Y.J. Sohn, D. Sebold, N. Karpstein, E. Spiecker, A. Kostka, O. Guillon, and R. Vaßen, Challenges of Single-Crystal CMSX-4 Repair Using Cold Spray, *Surf. Coat. Technol.*, 2025 https://doi.org/10.1016/j.surfcoat.2025.132368
43. M. Létang, S. Björklund, S. Joshi, D. Sebold, O. Guillon, and R. Vaßen, Repair of Single-Crystal CMSX-4 Using the High Velocity Air Fuel Process, *J Therm Spray Tech*, 2025 https://doi.org/10.1007/s11666-025-01944-2
44. T. Schwarz and H. Kockelmann, Die Bohrlochmethode–ein für Viele Anwendungsbereiche Optimales Verfahren zur Experimentellen Ermittlung von Eigenspannungen, *Messtech. Briefe*, 1993, **29**, p 33–38.
45. E. Kröner, Berechnung Der Elastischen Konstanten Des Vielkristalls Aus Den Konstanten Des Einkristalls, *Z. Phys.*, 1958, **151**, p 504–518. https://doi.org/10.1007/BF01337948
46. A. Epishin, B. Fedelich, M. Finn, G. Künecke, B. Rehmer, G. Nolze, C. Leistner, N. Petrushin, and I. Svetlov, Investigation of Elastic Properties of the Single-Crystal Nickel-Base Superalloy CMSX-4 in the Temperature Interval Between Room Temperature and 1300 °C, *Crystals*, 2021, **11**, 152. https://doi.org/10.3390/cryst11020152
47. DIN EN ISO 14916:2017-08, Thermisches Spritzen_- Ermittlung der Haftzugfestigkeit (ISO_14916:2017); Deutsche Fassung EN_ISO_14916:2017. https://doi.org/10.31030/2588875
48. M. Ramsperger, R.F. Singer, and C. Körner, Microstructure of the Nickel-Base Superalloy CMSX-4 Fabricated by Selective Electron Beam Melting, *Metall. Mater. Trans. A*, 2016, **47**(3), p 1469–1480. https://doi.org/10.1007/s11661-015-3300-y
49. D.M. Collins, N. D'Souza, C. Panwisawas, C. Papadaki, G.D. West, A. Kostka, and P. Kontis, Spinodal Decomposition Versus Classical Gamma-Prime Nucleation in a Nickel-Base Superalloy Powder: An in-Situ Neutron Diffraction and Atomic-Scale Analysis, *Acta Mater.*, 2020, **200**, p 959–970. https://doi.org/10.1016/j.actamat.2020.09.055
50. B. Wahlmann, F. Galgon, A. Stark, S. Gayer, N. Schell, P. Staron, and C. Körner, Growth, and Coarsening Kinetics of Gamma Prime Precipitates in CMSX-4 Under Simulated Additive Manufacturing Conditions, *Acta Mater.*, 2019, **180**, p 84–96. https://doi.org/10.1016/j.actamat.2019.08.049
51. Y. Cheng, X. Zhao, W. Xia, Q. Yue, Y. Gu, and Z. Zhang, The Overview of the Formation Mechanisms of Topologically Close-Packed Phases in Ni-Based Single Crystal Superalloys, *Mater. Des.*, 2024 https://doi.org/10.1016/j.matdes.2023.112582

52. J. Koßmann, C.H. Zenk, I. Lopez-Galilea, S. Neumeier, A. Kostka, S. Huth, W. Theisen, M. Göken, R. Drautz, and T. Hammerschmidt, Microsegregation and Precipitates of an as-Cast Co-Based Superalloy—Microstructural Characterization and Phase Stability Modelling, *J. Mater. Sci.*, 2015, **50**(19), p 6329–6338. https://doi.org/10.1007/s10853-015-9177-8
53. Y. Zou, W. Qin, E. Irissou, J.-G. Legoux, S. Yue, and J.A. Szpunar, Dynamic Recrystallization in the Particle/Particle Interfacial Region of Cold-Sprayed Nickel Coating: Electron Backscatter Diffraction Characterization, *Scripta Mater.*, 2009, **61**(9), p 899–902. https://doi.org/10.1016/j.scriptamat.2009.07.020
54. M. Saleh, V. Luzin, and K. Spencer, Analysis of the Residual Stress and Bonding Mechanism in the Cold Spray Technique Using Experimental and Numerical Methods, *Surf. Coat. Technol.*, 2014, **252**, p 15–28. https://doi.org/10.1016/j.surfcoat.2014.04.059
55. V. Luzin, K. Spencer, and M.-X. Zhang, Residual Stress and Thermo-Mechanical Properties of Cold Spray Metal Coatings, *Acta Mater.*, 2011, **59**(3), p 1259–1270. https://doi.org/10.1016/j.actamat.2010.10.058
56. Y.C. Tsui and T.W. Clyne, An Analytical Model for Predicting Residual Stresses in Progressively Deposited Coatings Part 1: Planar Geometry, *Thin Solid Films*, 1997, **306**, p 23–33. https://doi.org/10.1016/S0040-6090(97)00199-5
57. S.C. Cao, A.X. Guo, G. Wu, Y. Wang, J. Lu, and X. Zhang, A novel Multiple Impact Model for Predicting the Residual Stress State, *J. Mater. Res. Technol.*, 2023, **23**, p 4779–4789. https://doi.org/10.1016/j.jmrt.2023.02.060
58. G. Shayegan, H. Mahmoudi, R. Ghelichi, J. Villafuerte, J. Wang, M. Guagliano, and H. Jahed, Residual Stress Induced by Cold Spray Coating of Magnesium AZ31B Extrusion, *Mater. Des.*, 2014, **60**, p 72–84. https://doi.org/10.1016/j.matdes.2014.03.054